

Project 1: Pulse Monitor and Oximetry – Week 2

BE/EE/MedE 189a: Design and Construction of Biodevices

Fall 2017

Instructions

1. The lab is to be completed in groups of 2. Only one lab report is required per group.
2. Lab report
 - Include your VIs in your appendix
 - Write a brief outline of the lab including any modification/addition to the lab instructions.
 - Answer the post lab questions.
 - Emphasis is placed on the analysis and demonstration of understanding of the functionality, performance, and limitations of the system.

Procedure

Overview

In this project, we will use the principles discussed in the prelab to measure the pulse rate, before proceeding to additionally measure oxygenation next week. We will use a commercial oxygen sensor (Nellcor Oxisensor II D25) to measure the pulse rate. The Nellcor Oxisensor uses a DB9 connector (refer to Fig. 1 for pinout information). It can be directly connected to the ELVIS II breadboard. The oxisensor can be attached to your finger, as shown in Fig. 2. The oxisensor consists of a red LED, an infrared (IR) LED, and a photodiode to measure light signal from both LEDs. We will only use the red LED in our pulse monitor setup.

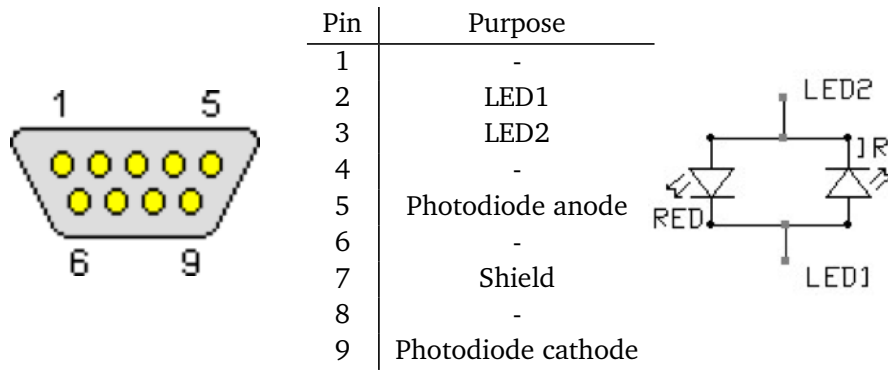


Figure 1: Nellcor Oxisensor II DB9 connector Pinout

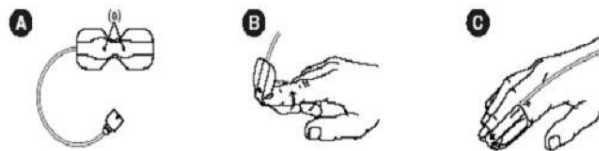


Figure 2: How to apply probe

Since the output of the photodiode is usually weak, we will build a simple amplifier to amplify the signal. We will then use the NI ELVIS II system and the LabVIEW program to acquire the amplified signal. Finally, the signal is processed in LabVIEW to get the pulse rate. An experiment we would like for you to explore is the possible change of the pulse rate when watching a flashing LED.

Constructing the circuit for Nellcore Oxisensor

The circuit for driving the red LED and the photodiode is shown in Fig. 3. Use the breadboard to construct the circuit and attach the oxisensor to your figure. Now try to detect the output of the signal using either a real or a virtual oscilloscope. Note that the signal will be very weak and it is hard to detect your pulse. However, the signal will fluctuate as you move your finger.

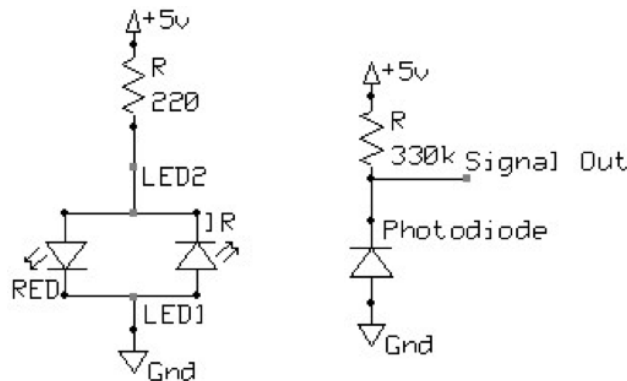


Figure 3: How to apply probe

Constructing the filter and amplification circuit

Use the circuit shown in Fig. 4, or any related circuit that you want, to filter and amplify the signal. Observe the signal using an oscilloscope. An example of the pulse signal is shown in Fig. 5.

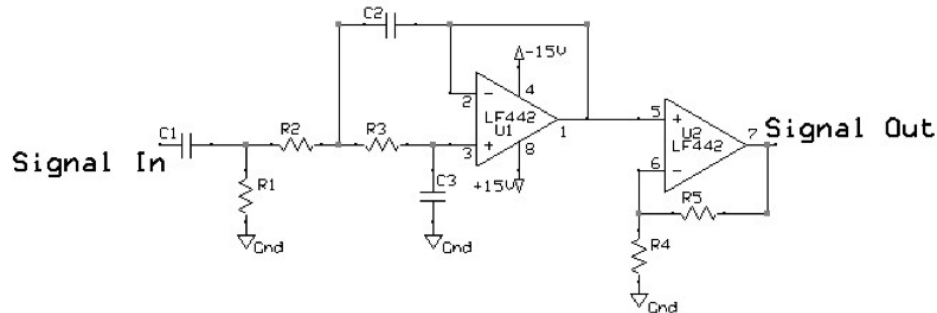


Figure 4: Filter and amplifier

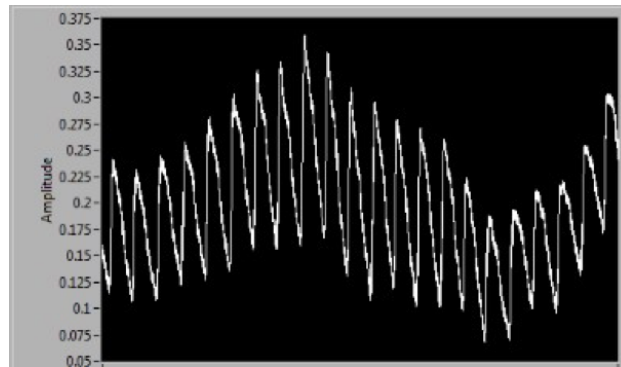


Figure 5: Example pluse signal

Here we will use two op-amps from LF442. Please see the attached datasheet for pin definitions. The signal should look similar to Fig. 5. Try the following parameters:

$$R1 = 150 \text{ k}\Omega$$

$$R4 = 10 \text{ k}\Omega$$

$$C1 = 2.2 \text{ }\mu\text{F}$$

$$C3 = 0.012 \text{ }\mu\text{F}$$

$$R2 = R3 = 1.8 \text{ M}\Omega$$

$$R5 = 1 \text{ M}\Omega$$

$$C2 = 0.027 \text{ }\mu\text{F}$$

Note: Resistors have no polarity so you can wire them up in any direction. Some capacitors have polarity, especially the high capacitance ones. The longer lead on the capacitor is the positive end—make sure you wire the capacitor such that the positive end faces the side of the circuit that is predominantly at a higher potential.

Write a LabVIEW VI for detecting and processing the signal

Use analog input DAQ to acquire the pulse signal. Write LabVIEW VIs to process the signal and extract and display the pulse rate.

Beat intervals and chaos. Surprisingly, in a healthy individual, the intervals between successive heartbeats vary in a rather chaotic manner. It has been reported that patients with congestive heart failure (CHF) have decreased cardiac chaos as compared to healthy individuals (see attached paper by Poon and Merrill, especially Fig. 1). CHF patients are found to have similar chaotic heartbeat interval except “frequently interrupted by periods of seemingly non-chaotic fluctuations.” Thus, a frequency spectrum (obtainable by FFT) will not sufficiently reveal these periods of regular heartbeat intervals (refer to Fig. 1c of Poon and Merrill). Improve your LabVIEW VI so that it is able to calculate beat intervals, plot them (essentially like in Fig. 1a of the paper) and detect periods of regular beat intervals. (Hint: You can test this using a simulated triangle wave as the beat interval trend of a CHF patient.)

Can you influence your pulse? Create a flashing virtual LED on a separate Labview VI. Make the LED flash at rates ranging from 60-120 flashes/minute. Looking at the LED and measuring your pulse rate using your previously built pulse monitor, find out if your pulse rate related to the flashing rate of the LED.

Post-lab questions

1. The circuit in Figure 4 consists of a first-order RC high pass filter, a Sallen-Key low pass filter and a non-inverting amplifier. Label which parts of the circuit correspond to each of these functions. Write down the low-pass and high-pass cut-off frequencies. Calculate the gain of the non-inverting amplifier.
2. What affects the accuracy of the pulse monitor that you have built?
3. What advantages does this pulse monitor have compared to other measures of cardiac function? What are its disadvantages?

morphology contradicts Rak's dichotomization of East and South African robust *Australopithecus*⁶.

It is possible that the KGA *A. boisei* population as a whole was morphologically distinct from that of the Turkana basin, despite a geographical proximity of approximately 200 km. The Konso macromammalian fauna exhibits significant differences from the Turkana counterparts at both 1.4 Myr and 1.9 Myr levels. Dominant bovids and suids at Konso include *Kobus* cf. *sigmoidalis*, *Damaliscus niro*, *Parmularius angusticornis*, a short-horned *Syncerus*, *Tragelaphus strepsiceros*, *Kolpochoerus majus*, *Kolpochoerus limnetes/olduvaiensis*, *Notochoerus* aff. *eutilus*, and *Metridiochoerus hopwoodi*. Most of these taxa are rare or absent at equivalent Turkana time horizons, or are different at the infraspecific level^{17,18}. Similarly, the abundant Acheulean assemblages found at KGA are lacking at East Turkana¹⁹. Thus, distinct differences between Konso and Turkana are seen in *A. boisei*, the fauna and archeological remains. Because all *Australopithecus* species hypodigms come from one dominant and a few subsidiary site samples, the extent of the polytypic nature of early hominid species may have been overlooked.

The importance of the Konso *A. boisei* fossils lies in their possession of uniquely derived features of that species, thus allowing secure taxonomic attribution at the species level, while otherwise extending the known range of *A. boisei* variation in many features. The striking deviations of the Konso morphology from the known Olduvai/Turkana *A. boisei* condition demonstrate that not all *A. boisei* features traditionally considered as part of a hyper-robust masticatory adaptation are of functional significance or decisive systematic value. This has important implications for early-hominid systematics and functional interpretations.

It is likely that many details of craniodental features used in evaluations of early hominids vary between populations in a manner consistent with random genetic drift. Excessive atomization of morphological features and their individual evaluations may then lead to erroneous phylogenetic and simplistic functional interpretations. We hypothesize that the facial morphology of the Konso skull, unique in the known *A. boisei* hypodigm, represents intraspecific variation, either individual, age-related, temporal and/or geographic. The striking distinctiveness of the Konso skull and the morphological trends common to both palates (KGA10-506 and KGA10-525) suggest that geographic variation is particularly influential. Geographically patterned, inter-basinal variation may be revealed further as more *A. boisei* specimens become available. Meanwhile, as some features once thought to characterize South African *A. robustus* are now shown to occur in East Africa, the case for robust *Australopithecus* monophyly is strengthened.

The taxonomic splitting of the ~2.0-Myr early-*Homo* hypodigm is a scheme rapidly gaining wide acceptance²⁰⁻²³, and the newly proposed taxon *Australopithecus bahrelghazali* has been claimed to be distinct from *A. afarensis*²⁴. These interpretations rely heavily on specimen-specific morphological differences. Such differences have been taken as indicating cladogenesis, but the Konso discoveries combined with modern anthropoid variation^{25,26} suggest that considerable morphological polymorphism and/or polytypism may have been present among all early hominids. Splitting of taxa at the species level, emphasizing minor morphological differences, would then be unwarranted. We predict that, as new hominid-bearing sedimentary basins are discovered and existing site samples are augmented, a more accurate picture of variation will emerge to challenge overly split phylogenies of hominid species. □

Received 10 June; accepted 9 September 1997.

1. Leakey, L. S. B. A new fossil skull from Olduvai. *Nature* **184**, 491-493 (1959).
2. Tobias, P. V. T. *Olduvai Gorge* Vol. 2, *The Cranium and Maxillary Dentition of Australopithecus (Zinjanthropus) boisei* (Cambridge Univ. Press, 1967).
3. Leakey, R. E. F. & Walker, A. New *Australopithecus boisei* specimens from East and West Lake Turkana, Kenya. *Am. J. Phys. Anthropol.* **76**, 1-24 (1988).
4. Wood, B. Koobi Fora Research Project Vol. 4 *Hominid Cranial Remains* (Clarendon, Oxford, 1991).
5. Brown, B., Walker, A., Ward, C. V. & Leakey, R. E. New *Australopithecus boisei* calvaria from East Lake Turkana, Kenya. *Am. J. Phys. Anthropol.* **91**, 137-159 (1993).
6. Rak, Y. *The Australopithecine Face* (Academic, New York, 1983).

7. Shipman, P. & Harris, J. M. in *Evolutionary History of the "Robust" Australopithecines* (ed. Grine, F.) 343-381 (de Gruyter, New York, 1988).
8. Asfaw, B. et al. The earliest Acheulean from Konso-Gardula. *Nature* **360**, 732-735 (1992).
9. Holloway, R. L. Human paleontological evidence relevant to language behaviour. *Hum. Neurobiol.* **2**, 105-114 (1983).
10. Suwa, G., White, T. D. & Howell, F. C. Mandibular postcanine dentition from the Shungura Formation, Ethiopia: Crown morphology, taxonomic allocations, and Plio-Pleistocene hominid evolution. *Am. J. Phys. Anthropol.* **101**, 247-282 (1996).
11. Walker, A., Leakey, R. E., Harris, J. M. & Brown, F. H. 2.5-Myr *Australopithecus boisei* from west of Lake Turkana. *Nature* **322**, 517-522 (1986).
12. Carney, J., Hill, A., Miller, J. & Walker, A. Late australopithecine from Baringo district, Kenya. *Nature* **230**, 509-514 (1971).
13. Gowlett, J. A. J., Harris, J. W. K., Walton, D. & Wood, B. A. Early archaeological sites, hominid remains and traces of fire from Chesowanja, Kenya. *Nature* **294**, 125-129 (1981).
14. Leakey, L. S. B. & Leakey, M. D. Recent discoveries of fossil hominids in Tanganyika at Olduvai and near Lake Natron. *Nature* **202**, 5-7 (1964).
15. Thouveny, N. & Taieb, M. Etude paleomagnetique des formations du Plio-Pleistocene de la Peninj (ouest du lac Natron, Tanzanie), limites de l'interpretation magnetostratigraphique. *Sci. Geol. Bull.* **40**, 57-70 (1987).
16. Wood, B., Wood, C. & Konigsberg, L. *Paranthropus boisei*: An example of evolutionary stasis? *Am. J. Phys. Anthropol.* **95**, 117-136 (1994).
17. Harris, J. M. *Koobi Fora Research Project* Vol. 2, *The Fossil Ungulates: Proboscidea, Perissodactyla, and Suidae* (Clarendon, Oxford, 1983).
18. Harris, J. M. *Koobi Fora Research Project* Vol. 3, *The Fossil Ungulates: Geology, Fossil Artiodactyls and Palaeoenvironments* (Clarendon, Oxford, 1991).
19. Leakey, M. G. & Leakey, R. E. *Koobi Fora Research Project* Vol. 1, *The Fossil Hominids and an Introduction to Their Context, 1968-1974* (Clarendon, Oxford, 1978).
20. Wood, B. Origin and evolution of the genus *Homo*. *Nature* **355**, 783-790 (1992).
21. Rightmire, G. P. Variation among early *Homo* crania from Olduvai Gorge and the Koobi Fora region. *Am. J. Phys. Anthropol.* **90**, 1-33 (1993).
22. Schrenk, F., Bromage, T. G., Betzler, C. G., Ring, U. & Juwayeyi, Y. Oldest *Homo* and Pliocene biogeography of the Malawi rift. *Nature* **365**, 833-836 (1993).
23. Kimbel, W. H., Johanson, D. C. & Rak, Y. Systematic assessment of a maxilla of *Homo* from Hadar, Ethiopia. *Am. J. Phys. Anthropol.* **103**, 235-262 (1997).
24. Brunet, M. et al. *Australopithecus bahrelghazali*, une nouvelle espèce d'Hominide ancien de la région de Koro Toro (Tchad). *C. R. Acad. Sci.* **322**, 907-913 (1996).
25. Albrecht, G. H. & Miller, J. in *Species, Species Concepts, and Primate Evolution* (eds Kimbel, W. H. & Martin, L. B.) 123-161 (Plenum, New York, 1993).
26. Uchida, A. *Peabody Museum Bulletin 4. Intra-species Variation among the Great Apes: Implications for Taxonomy of Fossil Hominoids* (Harvard Univ. Press, Cambridge, MA, 1996).
27. du Brul, E. L. Early Hominid feeding mechanisms. *Am. J. Phys. Anthropol.* **47**, 305-320 (1977).
28. Kimbel, W. H., White, T. D. & Johanson, D. C. in *Evolutionary History of the "Robust" Australopithecines* (ed. Grine, F.) 259-268 (de Gruyter, New York, 1988).
29. McCollum, M. A., Grine, F. E., Ward, S. C. & Kimbel, W. H. Subnasal morphological variation in extant hominoids and fossil hominids. *J. Hum. Evol.* **24**, 87-111 (1993).
30. WoldeGabriel, G. et al. Ecology and temporal placement of early Pliocene hominids at Aramis, Ethiopia. *Nature* **371**, 330-333 (1994).

Acknowledgements. The Konso Paleoanthropological Research Project has been conducted under permission from the Center for Research and Conservation of Cultural Heritage (CRCCH), Ministry of Information and Culture, Ethiopia. We thank the CRCCH and the National Museum of Ethiopia for allowing us to undertake our research; the Bureau of Culture and Information of the Southern Nations, Nationalities, and People's regional Government of Ethiopia for support; staff of the Bureau of Culture and Information and of CRCCH for participating in and contributing to the field research; A. Amzaye for discovering the KGA10-525 skull; the administration of the Konso Special Administration District and the Konso people for their support; A. Ademassu, T. Asseberwerk, T. Becker, H. Gilbert, C. Guillemot, Y. Haile-Selassie, F. C. Howell, B. Latimer, S. Simpson, M. Umer and Y. Zeleke for field participation, laboratory assistance, and/or suggestions; P. Snow for access to the LANL Geology/Geochemistry Group microprobe facility and assistance; and R. Holloway for the cranial-capacity estimate of KGA10-525. This work was funded by the Mitsubishi Foundation and the Japan Ministry of Education, Science, Sports and Culture.

Correspondence and requests for materials should be addressed to G.S. (suwa@biol.s.u-tokyo.ac.jp).

Decrease of cardiac chaos in congestive heart failure

Chi-Sang Poon & Christopher K. Merrill

Harvard-MIT Division of Health Sciences and Technology, Massachusetts Institute of Technology, Cambridge, Massachusetts 02139, USA

The electrical properties of the mammalian heart undergo many complex transitions in normal and diseased states¹⁻⁷. It has been proposed that the normal heartbeat may display complex nonlinear dynamics, including deterministic chaos^{8,9}, and that such cardiac chaos may be a useful physiological marker for the diagnosis¹⁰⁻¹² and management^{13,14} of certain heart trouble. However, it is not clear whether the heartbeat series of healthy and diseased hearts are chaotic or stochastic¹⁵⁻¹⁷, or whether cardiac chaos represents normal or abnormal behaviour¹⁸. Here we have used a highly sensitive technique, which is robust to random noise, to detect chaos¹⁹. We analysed the electrocardiograms from a group of healthy subjects and those with severe congestive heart failure (CHF), a clinical condition associated with a high risk of

sudden death. The short-term variations of beat-to-beat interval exhibited strongly and consistently chaotic behaviour in all healthy subjects, but were frequently interrupted by periods of seemingly non-chaotic fluctuations in patients with CHF. Chaotic dynamics in the CHF data, even when discernible, exhibited a high degree of random variability over time, suggesting a weaker form of chaos. These findings suggest that cardiac chaos is prevalent in healthy heart, and a decrease in such chaos may be indicative of CHF.

One of the main problems in studying the nonlinear dynamical behaviour of the heartbeat (and of any empirical time series in general) is the inevitable presence of random noise, which can often lead to false positive or negative identifications of chaos when traditional methods of nonlinear dynamics analysis are used. Although the effect of noise may be lessened to some extent by using long data records, this approach is limited by the possible non-stationarity of the heartbeat series^{20,21}.

To circumvent these difficulties, we have used a nonlinear systems identification technique¹⁹ to detect time-dependent and disease-dependent changes in the chaotic dynamics of the heartbeat. The technique identifies nonlinear determinism in a time series by iteratively generating a family of polynomial autoregressive models. The null hypothesis (namely, that the time series is stochastic with linear dynamics) is rejected if there is at least one nonlinear model that provides a significantly better fit to the data in a parsimonious manner than linear autoregressive models of all dynamical order. The statistical test is highly robust and sensitive, in that it is resistant to noise contamination and is applicable to short time series (with <1,000 points). This technique provides a highly specific test for deterministic chaos in that the null hypothesis is not readily rejected in the presence of random noise unless the underlying system is chaotic and/or has a fractal phase-space structure¹⁹. Indeed, simulation studies showed that the level of noise corruption that could be tolerated by such a chaotic test was directly related to the magnitude of the positive Lyapunov exponent, a measure of the degree of chaos in the underlying noise-free data (M. Barahona and

C.-S.P., unpublished observations). Moreover, the computational algorithm uses a recursive scheme for nonlinear systems identification and is highly efficient (typically, analysis of a 1,000-point time series takes just seconds on a desktop computer). The combination of specificity, sensitivity and computational efficiency of the chaotic test allowed a systematic statistical evaluation of the presence of deterministic chaos in multiple short segments of an extended heartbeat series, an analytical approach that would otherwise be impractical.

The data sets of interest were derived from an established database^{17,20,22} and consisted of continuous Holter records (at 128–250 samples s⁻¹) of heartbeat intervals from 8 healthy subjects and 11 CHF patients (age range, 22–71 years). At the time of the experiment, none of the subjects was on any medication that would affect the heart rate. To obviate possible non-physiological disturbances associated with wakefulness, data obtained only during nocturnal hours (totally 20,000 beats each) were used in the analysis. Subjects in both groups were selected on the basis of stability of the mean heart rate and limited number of ectopic beats and undetected beats. The heartbeat series were detrended using linear regression, but otherwise no preprocessing of the data was performed.

The heartbeat series of the CHF patients were characterized by the distinct presence of low-amplitude, low-frequency intermittent oscillations and decrease in temporal variability (Fig. 1), as reported previously^{22,23}. Generally, such an increase in regularity and decrease in temporal variability may reflect a decrease in either the noise or chaotic contents of the time series. To distinguish these possibilities, we first divided each heartbeat series into 40 contiguous short segments (of 500 beats each) to minimize the effect of non-stationarity of the data. We then applied the chaotic test to each data segment and evaluated the frequencies of linear and nonlinear episodes in each subject.

Nonlinear dynamics were manifested under the above test in both healthy and CHF heartbeat data (Fig. 2a, b). Because the chaotic test is conservative in the presence of noise (that is, predisposing to a

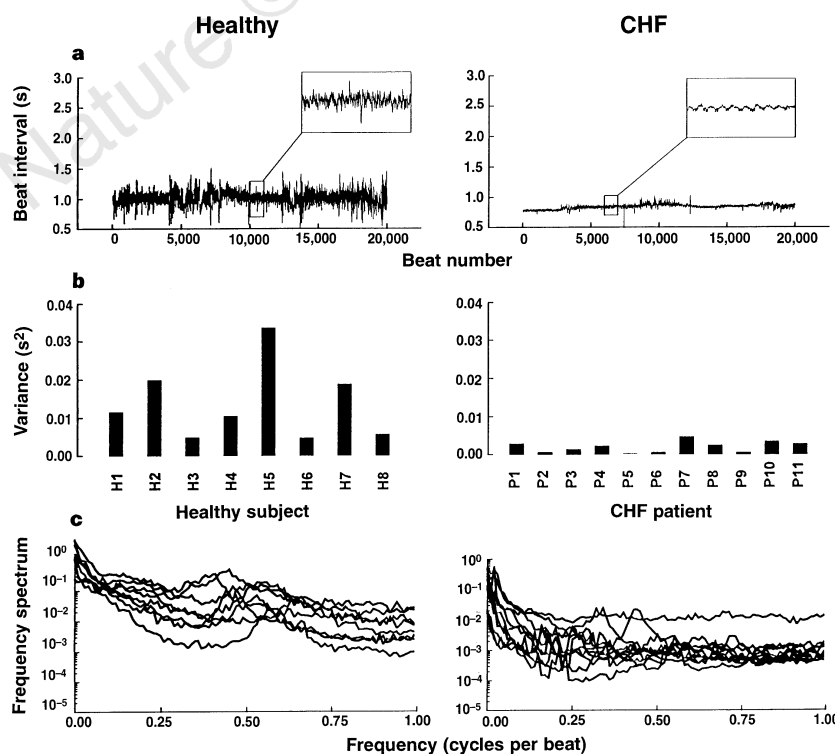


Figure 1 Characteristics of heartbeat data. **a**, Representative heartbeat series from a healthy subject (left) and a CHF patient (right). All heartbeat data were obtained during sleep and consisted of 20,000 beats. Insets show the self-similar character of the healthy heartbeat series and the decreased complexity and increased predictability of the CHF data in the form of low-amplitude, low-frequency intermittent oscillations. **b**, Variance of heartbeat intervals in all healthy subjects (left) and all CHF patients (right). Note the decreased variability of heartbeat in the CHF patient. **c**, Frequency spectrum of heartbeat intervals in all healthy subjects (left) and all CHF patients (right). Each frequency spectrum was obtained by taking a 2,000-point Fourier transform of the corresponding heartbeat series, averaged over all data segments, and then integrated over a 10-point bin in the frequency scale. The lack of sustained periodic or quasiperiodic components is indicated by the absence of frequency peaks in both subject groups.

linear model unless the data have a significant chaotic component), this finding suggests that the heartbeat series were intrinsically chaotic in both subject groups. The absence of other forms of nonlinear dynamics (such as limit cycles or invariant loops) is also indicated by the lack of constantly periodic or quasiperiodic components in the heartbeat series and corresponding frequency spectrum of all subjects (Fig. 1). Furthermore, the possible contribution of non-chaotic fractal attractors to the nonlinear dynamics may also be excluded, as such attractors occur only under certain special circumstances²⁴, which are unlikely in the cardiac system.

However, deterministic chaos was detected consistently in nearly

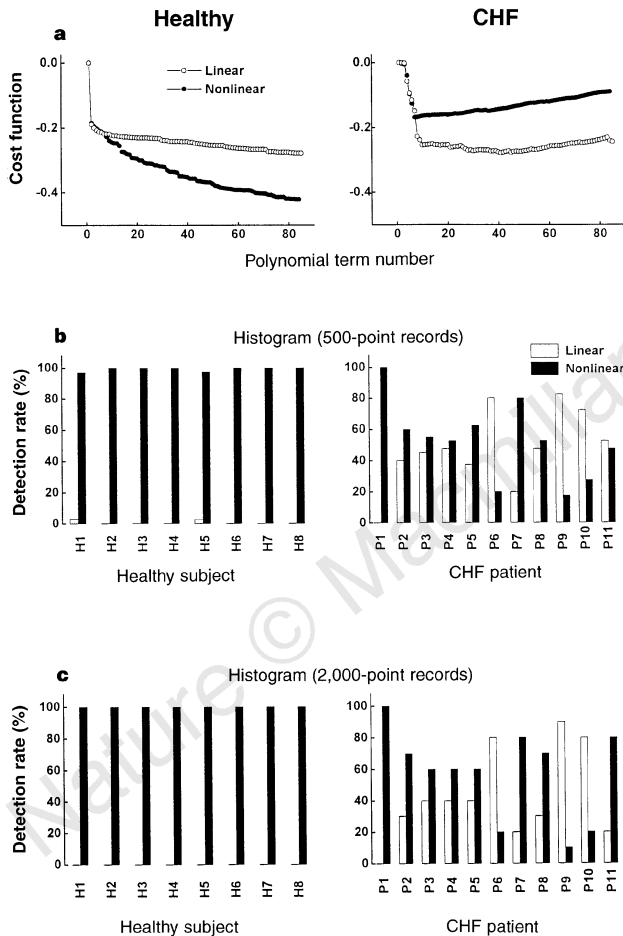


Figure 2 Chaos analysis of heartbeat series. The data were fitted with dynamical models of linear and polynomial forms with increasing order. Nonlinear dynamics was indicated if the best nonlinear model provides a better fit to the data than the best linear model with a similar number of polynomial terms. Model selection was based upon the *F*-ratio test for residuals at the 1% significance level. This technique is conservative in that it predisposes to a linear model (null hypothesis) in the presence of random noise unless the system is chaotic¹⁹. **a**, Examples of linear and nonlinear model fits of a 500-beat data segment for the same healthy subject (left) and CHF patient (right) shown in Fig. 1a. The cost function is of the form¹⁹: $C(r) = \log_e \epsilon(r) + r/N$, where r is the number of polynomial terms, $\epsilon(r)$ is the residual error, and N is the length of the time series. Both the cost function and the *F*-ratio test yielded a nonlinear model for the healthy subject and a linear model for the CHF subject. **b**, Histograms of linear and nonlinear model selection for all 500-beat data segments based on the above test in healthy subjects (left) and CHF patients (right). Note the high detection rates for chaos (nearly 100%) in the healthy group and the relatively low detection rates in CHF group (except patient P1). **c**, As **b**, but using 2,000-beat data segments.

all data segments in the healthy group, but the detection rate was markedly decreased (by 20–80%) in all but one of the CHF patients (Fig. 2b). Because all data were from subjects during nocturnal hours, and the CHF data were even less variable than the normal data (Fig. 1), it is highly unlikely that the low detection rate in the CHF group was caused by increased noise corruption. To confirm this, we repeated the test with data segments of 2,000 beats each to increase the signal content. Again, all healthy heartbeat data with the longer segmentation proved strongly chaotic, but the corresponding CHF data still exhibited relatively low detection rates (Fig. 2c). Because a weakly chaotic time series is generally more susceptible to noise corruption than is a strongly chaotic one (one with a large positive Lyapunov exponent), the low detection rate in the CHF group suggests that the intensity of cardiac chaos was decreased in CHF patients.

Another way of measuring the changes in intensity of chaos in a noise-corrupted time series is to compare the variability of the resulting nonlinear models for those data segments that tested positive for deterministic chaos. Again, we make use of the property that the chaotic dynamics in a noise-corrupted time series is more readily identifiable if it has a higher signal-to-noise ratio. Thus the nonlinear coefficient estimates for the CHF data are expected to be less variable if the lower temporal variability of the CHF data (Fig. 1) reflected a decrease in noise level instead of a decrease in chaotic content.

To test this hypothesis, we computed the nonlinear coefficients for all chaotic segments of the healthy and CHF heartbeat series. Indeed, the estimated nonlinear coefficients were considerably more variable in the CHF patients than in healthy subjects (Fig. 3). This criterion again held in all but one of the CHF patients and for the group as a whole. The increased parameter variability in the CHF group, together with a corresponding decrease in detection rate for

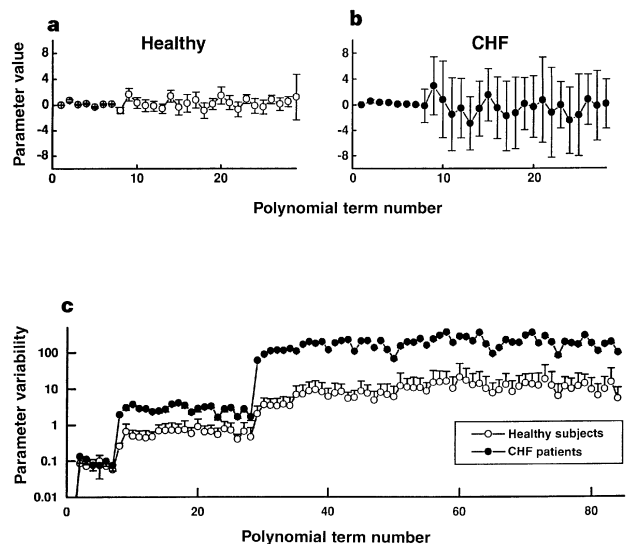


Figure 3 Variability of parameter estimates corresponding to all 500-beat data segments that were identified as chaotic in Fig. 2. Data shown are estimates of the leading nonlinear coefficients (mean \pm s.d.) from the same healthy subject (**a**) and CHF patient (**b**) shown in Fig. 1a. Note the increased variability (s.d.) of estimated coefficients in the CHF patient. **c**, Average s.d. values (mean \pm s.e.) of the first 80 nonlinear coefficient estimates for the healthy and CHF groups are plotted on a semi-logarithmic scale. The parameter estimates were significantly more variable in the CHF group than in the healthy group. All CHF patients except P1 exhibited similar increased parameter variability.

chaos (Fig. 2), confirm that the degree of cardiac chaos was decreased in the CHF patients.

These critical tests strongly support the suggested prevalence of cardiac chaos in healthy subjects^{8,9}. Moreover, our results indicate that cardiac chaos persists in CHF patients, albeit less strongly than in healthy subjects. The intermittent heartbeat oscillations characteristic of these patients²² (Fig. 1) suggest that they may be at the brink of intermittency, a common route to and out of chaos²⁵. Whereas the effect of noise contamination of the data precluded the reliable detection of chaos with previous approaches, we have used this property to evaluate statistically the changes in cardiac chaos with heart disease. Such a statistical approach has been made possible by the sensitivity, specificity and computational efficiency of the chaotic test¹⁹.

Our results do not reveal the mechanisms of cardiac chaos and its recession in heart failure; indeed abnormalities in left ventricular and autonomic system functions may all contribute to a decrease in complexity of the heartbeat nonlinear dynamics in CHF patients²². Nevertheless, of all the subjects tested, only one CHF patient failed both diagnostic criteria, corresponding to a type-I and type-II diagnostic error of 9% and 0%, respectively. Such remarkable consistency of the chaotic tests, together with the efficiency of the computational algorithm, suggest that such indices of chaos may be used as a specific, non-invasive and on-line diagnostic test for heart disease, and a possible indicator of imminent ventricular fibrillation²⁶. □

Received 20 May; accepted 1 August 1997.

- Smith, J. M. & Cohen, R. J. Simple finite-element model accounts for wide range of cardiac dysrhythmias. *Proc. Natl Acad. Sci. USA* **81**, 233–237 (1984).
- Chialvo, D. R. & Jalife, J. Nonlinear dynamics of cardiac excitation and impulse propagation. *Nature* **330**, 749–752 (1987).
- Chialvo, D. R., Gilmour, R. F. & Jalife, J. Low-dimensional chaos in cardiac tissue. *Nature* **343**, 653–657 (1990).
- Jalife, J. *Ann. NY Acad. Sci.* **591** (1990).
- Davidenko, J. M., Pertsov, R. S., Baxter, W. & Jalife, J. Stationary and drifting spiral waves of excitation in isolated cardiac muscle. *Nature* **335**, 349–351 (1989).
- Winfree, A. T. Electrical turbulence in three-dimensional heart muscle. *Science* **266**, 1003–1006 (1994).
- Glass, L. Dynamics of cardiac arrhythmias. *Phys. Today* **40–45** (1996).
- Goldberger, A. L. Is the normal heartbeat chaotic or homeostatic? *News Physiol. Sci.* **6**, 87–91 (1991).
- Sugihara, G., Allan, W., Sobel, D. & Allan, K. D. Nonlinear control of heart rate variability in human infants. *Proc. Natl Acad. Sci. USA* **93**, 2608–2613 (1996).
- Denton, T. A., Diamond, G. A., Helfant, R. H., Khan, S. & Karagueuzian, H. Fascinating rhythm: A primer on chaos theory and its application to cardiology. *Am. Heart J.* **120**, 1419–1440 (1990).
- Skinner, J. E., Goldberger, A. L., Mayer-Kress, G. & Ideker, R. E. Chaos in the heart: Implications for clinical cardiology. *Biotechnology* **8**, 1018–1024 (1990).
- Goldberger, A. L. Nonlinear dynamics for clinicians: Chaos theory, fractals and complexity at the bedside. *Lancet* **347**, 1312–1314 (1996).
- Garfinkel, A., Spano, M. L., Ditto, W. L. & Weiss, J. N. Controlling cardiac chaos. *Science* **257**, 1230–1235 (1992).
- Garfinkel, A., Weiss, J. N., Ditto, W. L. & Spano, M. L. Chaos control of cardiac arrhythmias. *Trends Cardiovasc. Med.* **5**, 76–80 (1995).
- Kaplan, D. T. & Cohen, R. J. Is fibrillation chaos? *Circ. Res.* **67**, 886–892 (1990).
- Kanters, J. K., Holstein-Rathlou, N.-H. & Agner, E. Lack of evidence for low-dimensional chaos in heart rate variability. *J. Cardiovasc. Electrophysiol.* **5**, 591–601 (1994).
- Turcott, R. G. & Teich, M. C. Fractal character of the electrocardiogram: Distinguishing heart-failure and normal patients. *Ann. Biomed. Eng.* **24**, 269–293 (1996).
- Glass, L. Is cardiac chaos normal or abnormal? *J. Cardiovasc. Electrophysiol.* **1**, 481–482 (1990).
- Barahona, M. & Poon, C.-S. Detection of nonlinear dynamics in short, noisy time series. *Nature* **381**, 215–217 (1996).
- Peng, C. K., Havlin, S., Stanley, H. E. & Goldberger, A. L. Quantification of scaling exponents and crossover phenomena in nonstationary heartbeat time series. *Chaos* **5**, 82–87 (1995).
- Ivanov, P. C. *et al.* Scaling behaviour of heartbeat intervals obtained by wavelet-based time-series analysis. *Nature* **383**, 323–327 (1996).
- Goldberger, A. L., Rigney, D. R., Mietus, J., Antman, E. W. & Greenwald, S. Nonlinear dynamics in sudden cardiac death syndrome: heart rate oscillations and bifurcations. *Experientia* **44**, 983–987 (1988).
- Casolo, G., Balli, E., Taddei, T., Amuhasi, J. & Gori, C. Decreased spontaneous heart rate variability on congestive heart failure. *Am. J. Cardiol.* **64**, 1162–1167 (1989).
- Grebogi, C., Ott, E., Pelikan, S. & Yorke, J. A. Strange attractors that are not chaotic. *Physica D* **13**, 261–268 (1984).
- Pomeau, Y. & Manneville, P. Intermittent transition to turbulence in dissipative dynamical systems. *Commun. Math. Phys.* **74**, 189–197 (1980).
- Skinner, J. E., Pratt, C.-M. & Vybiral, T. A. Reduction in the correlation dimension of heartbeat intervals precedes imminent ventricular fibrillation in human subjects. *Am. Heart J.* **125**, 731–743 (1993).

Acknowledgements. We thank A. L. Goldberger and R. G. Mark for discussions and comments on the manuscript, and A. L. Goldberger and J. E. Mietus for providing the heartbeat data. This work was supported by grants from the National Heart, Lung and Blood Institute, National Science Foundation, and Office of Naval Research.

Correspondence and requests for materials should be addressed to C.-S.P. (e-mail: cpoon@mit.edu).

A specific neural substrate for perceiving facial expressions of disgust

M. L. Phillips*, A. W. Young†, C. Senior*, M. Brammer‡, C. Andrews§, A. J. Calder†, E. T. Bullmore‡, D. I. Perrett||, D. Rowland||, S. C. R. Williams§, J. A. Gray† & A. S. David*

* Department of Psychological Medicine, King's College School of Medicine and Dentistry and Institute of Psychiatry, 103 Denmark Hill, London SE5 8AZ, UK

† Applied Psychology Unit, 15 Chaucer Road, Cambridge CB2 2EF, UK

‡ Neuroimaging Unit, § Brain Image Analysis Unit, ¶ Department of Psychology, Institute of Psychiatry, De Crespigny Park, London SE5 8AF, UK

|| School of Psychology, University of St Andrews, Fife KY16 9JU, UK

Recognition of facial expressions is critical to our appreciation of the social and physical environment, with separate emotions having distinct facial expressions¹. Perception of fearful facial expressions has been extensively studied, appearing to depend upon the amygdala^{2–6}. Disgust—literally ‘bad taste’—is another important emotion, with a distinct evolutionary history⁷, and is conveyed by a characteristic facial expression^{8–10}. We have used functional magnetic resonance imaging (fMRI) to examine the neural substrate for perceiving disgust expressions. Normal volunteers were presented with faces showing mild or strong disgust or fear. Cerebral activation in response to these stimuli was contrasted with that for neutral faces. Results for fear generally confirmed previous positron emission tomography findings of amygdala involvement. Both strong and mild expressions of disgust activated anterior insular cortex but not the amygdala; strong disgust also activated structures linked to a limbic cortico–striatal–thalamic circuit. The anterior insula is known to be involved in responses to offensive tastes. The neural response to facial expressions of disgust in others is thus related to appraisal of distasteful stimuli.

We aimed to demonstrate distinct neural substrates for perception of two emotions, fear and disgust, replicating previous observations of a link between fear perception and amygdala activation^{5,6}, and examining the substrate for perception of disgust. It was postulated that perception of facial expressions of disgust would involve structures implicated in the appreciation of offensive stimuli. A cortico–striatal–thalamic circuit has been identified in primates¹¹, which may be involved in responses to emotive stimuli. There is clinical evidence for the probable involvement of some of these structures in appreciation of disgust: impaired recognition of disgust from facial expressions has been reported both in patients with symptomatic Huntington's disease¹², and presymptomatic carriers of the Huntington's gene¹³.

Subjects viewed grey-scale pictures of faces from a standard set¹⁴ depicting disgusted, fearful and neutral expressions. There were two levels of intensity (75 and 150%) for the facial expressions of disgust and fear for each individual face, and one level for the neutral expression, all produced by computer graphical manipulation of the prototype of each expression¹⁵ (Fig. 1). As a neutral face, we used an image with a slightly (25%) happy expression (see Methods). Subjects viewed blocks of emotional (disgusted or fearful) faces alternating with neutral faces in blocks. There were four separate experiments, in a randomized order, incorporating an alternating (neutral/emotional) design for each emotion (fear/disgust) and intensity of expression (mild, 75%; strong, 150%). After presentation of each face, subjects made a decision as to its sex by pressing one of two buttons with the right thumb. The sex decision task was chosen to allow an identical task and response across all conditions, and to permit comparison to a previous study of fear which also

LF442

Dual Low Power JFET Input Operational Amplifier

General Description

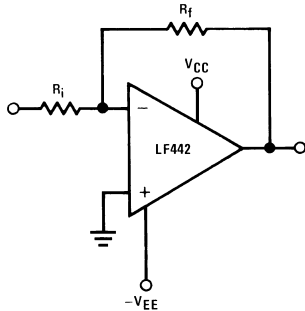
The LF442 dual low power operational amplifiers provide many of the same AC characteristics as the industry standard LM1458 while greatly improving the DC characteristics of the LM1458. The amplifiers have the same bandwidth, slew rate, and gain (10 kΩ load) as the LM1458 and only draw one tenth the supply current of the LM1458. In addition the well matched high voltage JFET input devices of the LF442 reduce the input bias and offset currents by a factor of 10,000 over the LM1458. A combination of careful layout design and internal trimming guarantees very low input offset voltage and voltage drift. The LF442 also has a very low equivalent input noise voltage for a low power amplifier.

The LF442 is pin compatible with the LM1458 allowing an immediate 10 times reduction in power drain in many applications. The LF442 should be used where low power dissipation and good electrical characteristics are the major considerations.

Features

- 1/10 supply current of a LM1458: 400 μA (max)
- Low input bias current: 50 pA (max)
- Low input offset voltage: 1 mV (max)
- Low input offset voltage drift: 10 μV/°C (max)
- High gain bandwidth: 1 MHz
- High slew rate: 1 V/μs
- Low noise voltage for low power: 35 nV/√Hz
- Low input noise current: 0.01 pA/√Hz
- High input impedance: 10¹²Ω
- High gain V_O = ±10V, R_L = 10k: 50k (min)

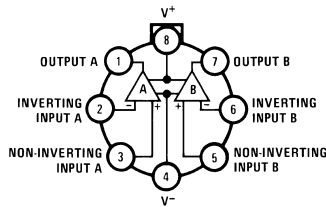
Typical Connection



00915501

Connection Diagrams

Metal Can Package



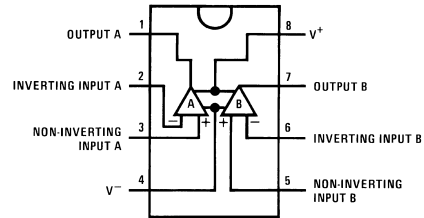
00915502

Pin 4 connected to case

Top View

Order Number LF442AMH or LF442MH/883
See NS Package Number H08A

Dual-In-Line Package



00915504

Top View

Order Number LF442ACN or LF442CN
See NS Package Number N08E

Ordering Information

LF442XYZ

X indicates electrical grade

Y indicates temperature range

“M” for military

“C” for commercial

Z indicates package type

“H” or “N”

Absolute Maximum Ratings (Note 1)

If Military/Aerospace specified devices are required, please contact the National Semiconductor Sales Office/Distributors for availability and specifications.

	LF442A	LF442
Supply Voltage	±22V	±18V
Differential Input Voltage	±38V	±30V
Input Voltage Range (Note 2)	±19V	±15V
Output Short Circuit Duration (Note 3)	Continuous	Continuous
T_j max	H Package 150°C	N Package 115°C

	H Package	N Package
θ_{JA} (Typical) (Note 4)	65°C/W	114°C/W
(Note 5)	165°C/W	152°C/W
θ_{JC} (Typical)	21°C/W	
Operating Temperature Range	(Note 5)	(Note 5)
Storage Temperature Range	-65°C ≤ T _A ≤ 150°C -65°C ≤ T _A ≤ 150°C	
Lead Temperature (Soldering, 10 sec.)	260°C	260°C
ESD Tolerance	Rating to be determined	

DC Electrical Characteristics (Note 7)

Symbol	Parameter	Conditions	LF442A			LF442			Units
			Min	Typ	Max	Min	Typ	Max	
V _{OS}	Input Offset Voltage	R _S = 10 kΩ, T _A = 25°C		0.5	1.0		1.0	5.0	mV
		Over Temperature						7.5	mV
ΔV _{OS} /ΔT	Average TC of Input Offset Voltage	R _S = 10 kΩ		7	10		7		μV/°C
I _{OS}	Input Offset Current	V _S = ±15V (Notes 7, 8)	T _j = 25°C	5	25		5	50	pA
			T _j = 70°C		1.5			1.5	nA
			T _j = 125°C		10				nA
I _B	Input Bias Current	V _S = ±15V (Notes 7, 8)	T _j = 25°C	10	50		10	100	pA
			T _j = 70°C		3			3	nA
			T _j = 125°C		20				nA
R _{IN}	Input Resistance	T _j = 25°C		10 ¹²			10 ¹²		Ω
A _{VOL}	Large Signal Voltage Gain	V _S = ±15V, V _O = ±10V, R _L = 10 kΩ, T _A = 25°C	50	200		25	200		V/mV
		Over Temperature	25	200		15	200		V/mV
V _O	Output Voltage Swing	V _S = ±15V, R _L = 10 kΩ	±12	±13		±12	±13		V
V _{CM}	Input Common-Mode Voltage Range		±16	+18 -17		±11	+14 -12		V V
CMRR	Common-Mode Rejection Ratio	R _S ≤ 10 kΩ	80	100		70	95		dB
PSRR	Supply Voltage Rejection Ratio	(Note 9)	80	100		70	90		dB
I _S	Supply Current			300	400		400	500	μA

AC Electrical Characteristics (Note 7)

Symbol	Parameter	Conditions	LF442A			LF442			Units
			Min	Typ	Max	Min	Typ	Max	
	Amplifier to Amplifier Coupling	$T_A = 25^\circ\text{C}$, $f = 1 \text{ Hz-20 kHz}$ (Input Referred)		-120			-120		dB
SR	Slew Rate	$V_S = \pm 15\text{V}$, $T_A = 25^\circ\text{C}$	0.8	1		0.6	1		V/ μs
GBW	Gain-Bandwidth Product	$V_S = \pm 15\text{V}$, $T_A = 25^\circ\text{C}$	0.8	1		0.6	1		MHz
e_n	Equivalent Input Noise Voltage	$T_A = 25^\circ\text{C}$, $R_S = 100\Omega$, $f = 1 \text{ kHz}$		35			35		nV/ $\sqrt{\text{Hz}}$
i_n	Equivalent Input Noise Current	$T_A = 25^\circ\text{C}$, $f = 1 \text{ kHz}$		0.01			0.01		pA/ $\sqrt{\text{Hz}}$

Note 1: "Absolute Maximum Ratings" indicate limits beyond which damage to the device may occur. Operating Ratings indicate conditions for which the device is functional, but do not guarantee specific performance limits.

Note 2: Unless otherwise specified the absolute maximum negative input voltage is equal to the negative power supply voltage.

Note 3: Any of the amplifier outputs can be shorted to ground indefinitely, however, more than one should not be simultaneously shorted as the maximum junction temperature will be exceeded.

Note 4: The value given is in 400 linear feet/min air flow.

Note 5: The value given is in static air.

Note 6: These devices are available in both the commercial temperature range $0^\circ\text{C} \leq T_A \leq 70^\circ\text{C}$ and the military temperature range $-55^\circ\text{C} \leq T_A \leq 125^\circ\text{C}$. The temperature range is designated by the position just before the package type in the device number. A "C" indicates the commercial temperature range and an "M" indicates the military temperature range. The military temperature range is available in "H" package only.

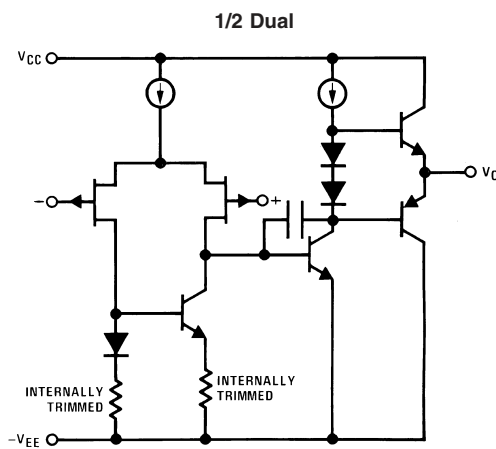
Note 7: Unless otherwise specified, the specifications apply over the full temperature range and for $V_S = \pm 20\text{V}$ for the LF442A and for $V_S = \pm 15\text{V}$ for the LF442. V_{OS} , I_B , and I_{OS} are measured at $V_{CM} = 0$.

Note 8: The input bias currents are junction leakage currents which approximately double for every 10°C increase in the junction temperature, T_j . Due to limited production test time, the input bias currents measured are correlated to junction temperature. In normal operation the junction temperature rises above the ambient temperature as a result of internal power dissipation, P_D . $T_j = T_A + \theta_{JA}P_D$ where θ_{JA} is the thermal resistance from junction to ambient. Use of a heat sink is recommended if input bias current is to be kept to a minimum.

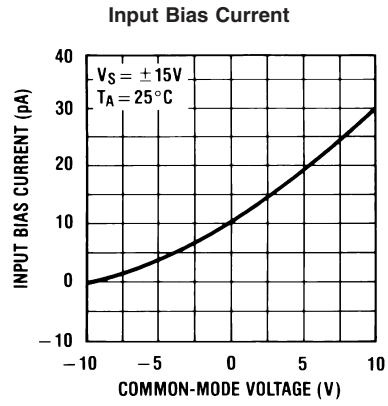
Note 9: Supply voltage rejection ratio is measured for both supply magnitudes increasing or decreasing simultaneously in accordance with common practice from $\pm 15\text{V}$ to $\pm 5\text{V}$ for the LF442 and $\pm 20\text{V}$ to $\pm 5\text{V}$ for the LF442A.

Note 10: Refer to RETS442X for LF442MH military specifications.

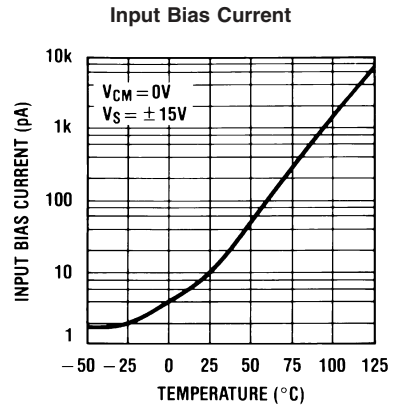
Simplified Schematic



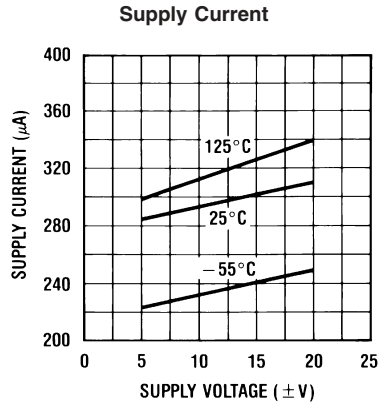
Typical Performance Characteristics



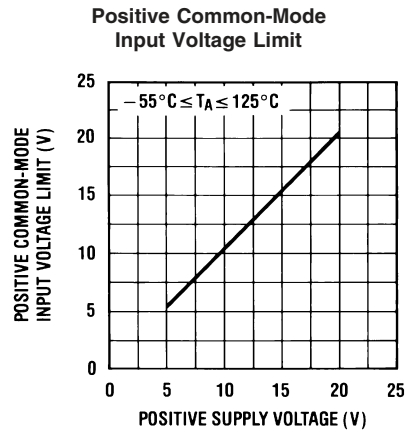
00915517



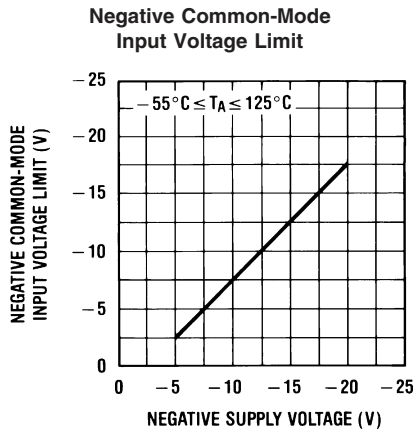
00915518



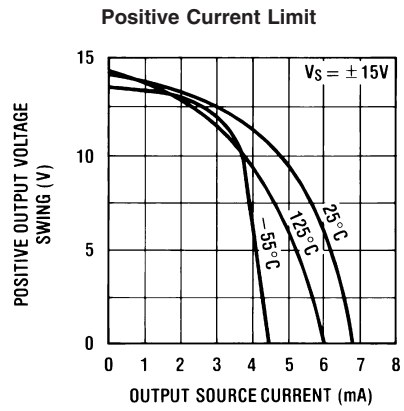
00915519



00915520

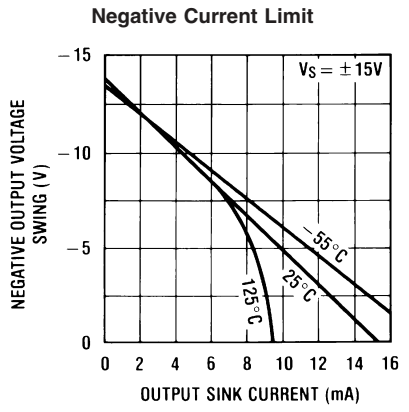


00915521

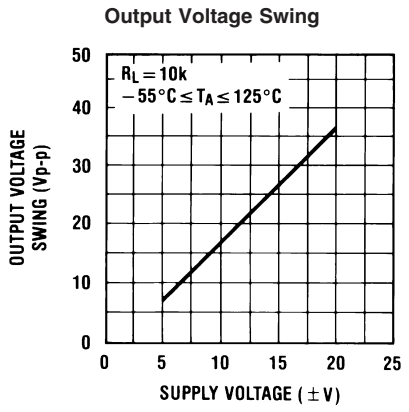


00915522

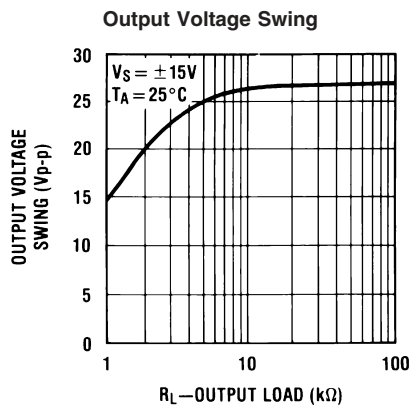
Typical Performance Characteristics (Continued)



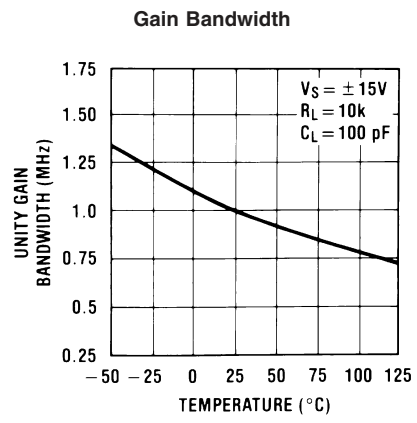
00915523



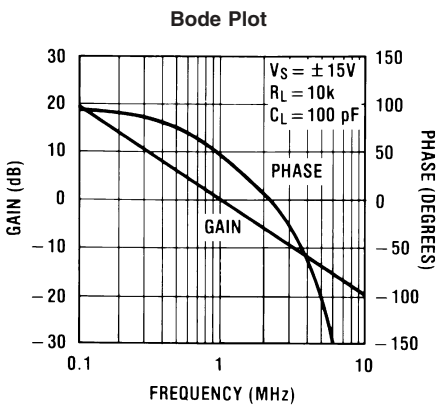
00915524



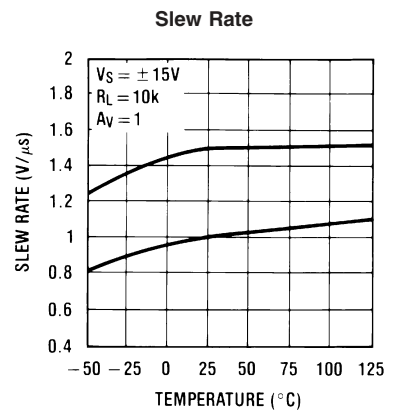
00915525



00915526



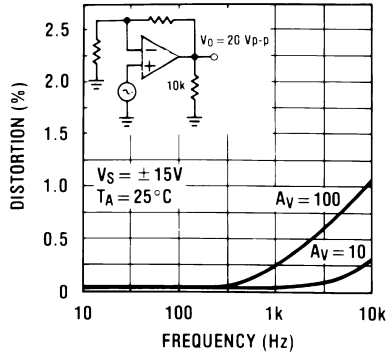
00915527



00915528

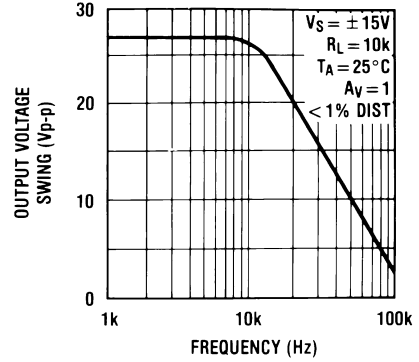
Typical Performance Characteristics (Continued)

Distortion vs Frequency



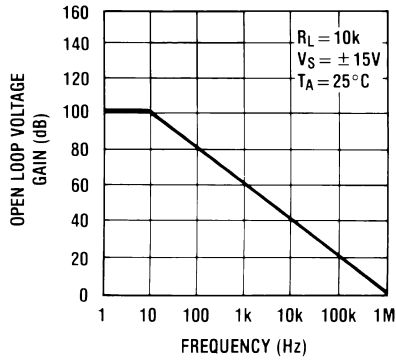
00915529

Undistorted Output Voltage Swing



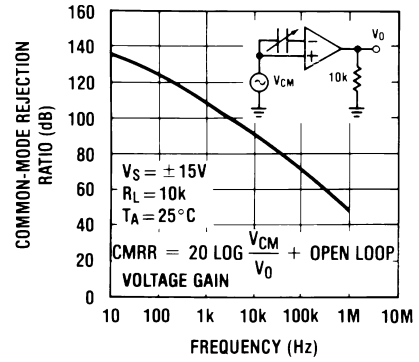
00915530

Open Loop Frequency Response



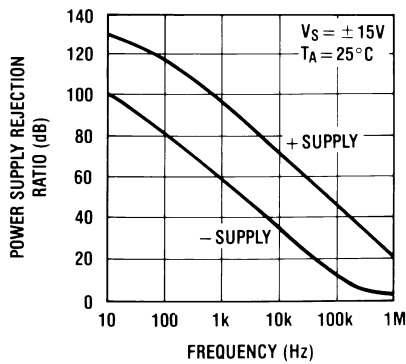
00915531

Common-Mode Rejection Ratio



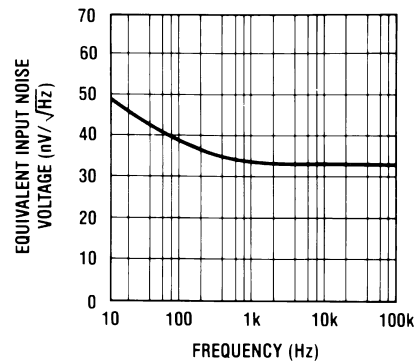
00915532

Power Supply Rejection Ratio



00915533

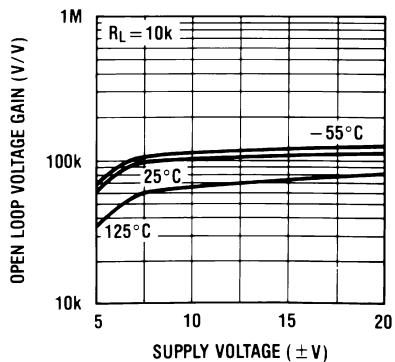
Equivalent Input Noise Voltage



00915534

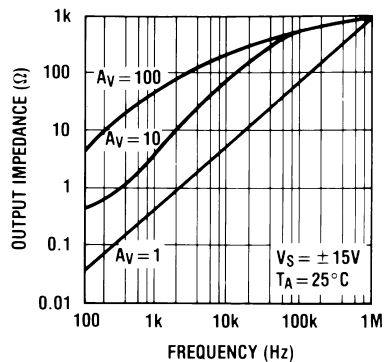
Typical Performance Characteristics (Continued)

Open Loop Voltage Gain



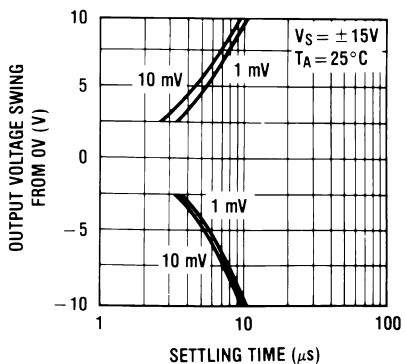
00915535

Output Impedance



00915536

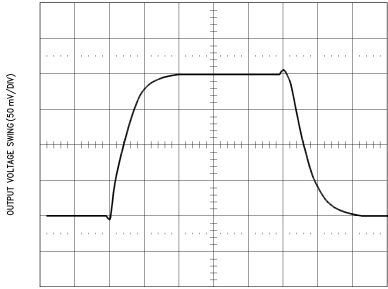
Inverter Settling Time



00915537

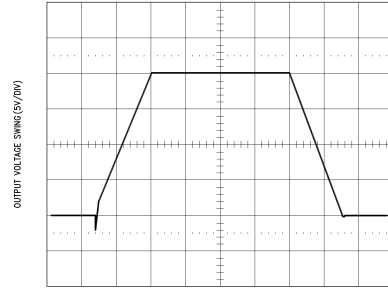
Pulse Response $R_L = 10\text{ k}\Omega, C_L = 10\text{ pF}$

Small Signal Inverting



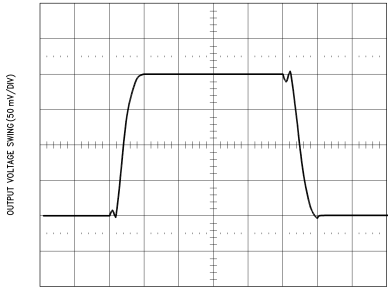
00915507

Large Signal Inverting



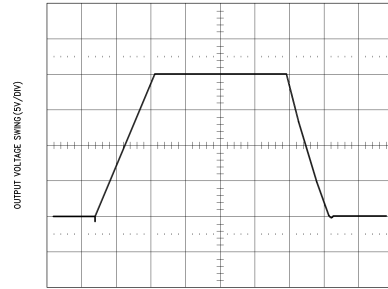
00915509

Small Signal Non-Inverting



00915508

Large Signal Non-Inverting



00915510

Application Hints

This device is a dual low power op amp with internally trimmed input offset voltages and JFET input devices (BI-FET II). These JFETs have large reverse breakdown voltages from gate to source and drain eliminating the need for clamps across the inputs. Therefore, large differential input voltages can easily be accommodated without a large increase in input current. The maximum differential input voltage is independent of the supply voltages. However, neither of the input voltages should be allowed to exceed the negative supply as this will cause large currents to flow which can result in a destroyed unit.

Exceeding the negative common-mode limit on either input will force the output to a high state, potentially causing a reversal of phase to the output. Exceeding the negative common-mode limit on both inputs will force the amplifier output to a high state. In neither case does a latch occur since raising the input back within the common-mode range again puts the input stage and thus the amplifier in a normal operating mode.

Exceeding the positive common-mode limit on a single input will not change the phase of the output; however, if both inputs exceed the limit, the output of the amplifier will be forced to a high state.

The amplifiers will operate with a common-mode input voltage equal to the positive supply; however, the gain bandwidth and slew rate may be decreased in this condition. When the negative common-mode voltage swings to within 3V of the negative supply, an increase in input offset voltage may occur.

Each amplifier is individually biased to allow normal circuit operation with power supplies of $\pm 3.0V$. Supply voltages less than these may degrade the common-mode rejection and restrict the output voltage swing.

The amplifiers will drive a 10 k Ω load resistance to $\pm 10V$ over the full temperature range.

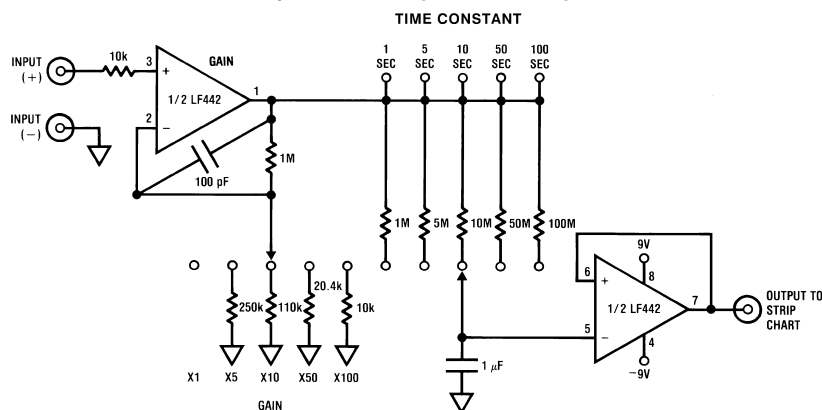
Precautions should be taken to ensure that the power supply for the integrated circuit never becomes reversed in polarity or that the unit is not inadvertently installed backwards in a socket as an unlimited current surge through the resulting forward diode within the IC could cause fusing of the internal conductors and result in a destroyed unit.

As with most amplifiers, care should be taken with lead dress, component placement and supply decoupling in order to ensure stability. For example, resistors from the output to an input should be placed with the body close to the input to minimize "pick-up" and maximize the frequency of the feedback pole by minimizing the capacitance from the input to ground.

A feedback pole is created when the feedback around any amplifier is resistive. The parallel resistance and capacitance from the input of the device (usually the inverting input) to AC ground set the frequency of the pole. In many instances the frequency of this pole is much greater than the expected 3 dB frequency of the closed loop gain and consequently there is negligible effect on stability margin. However, if the feedback pole is less than approximately 6 times the expected 3 dB frequency a lead capacitor should be placed from the output to the input of the op amp. The value of the added capacitor should be such that the RC time constant of this capacitor and the resistance it parallels is greater than or equal to the original feedback pole time constant.

Typical Applications

Battery Powered Strip Chart Preamplifier



00915511

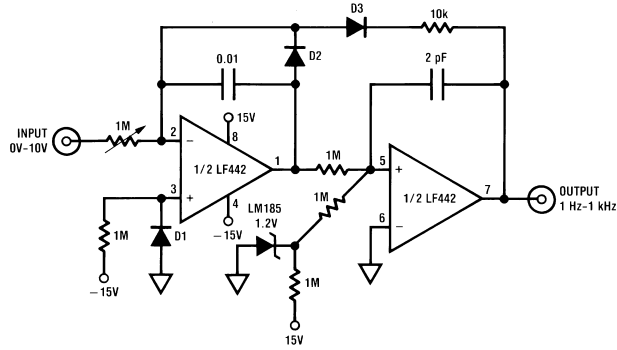
Runs from 9v batteries ($\pm 9V$ supplies)

Fully settable gain and time constant

Battery powered supply allows direct plug-in interface to strip chart recorder without common-mode problems

Typical Applications (Continued)

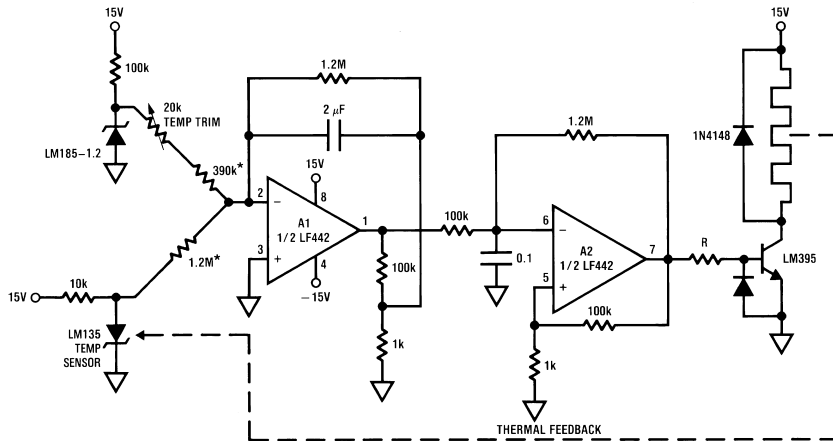
“No FET” Low Power V→F Converter



00915512

- Trim 1M pot for 1 kHz full-scale output
- 15 mW power drain
- No integrator reset FET required
- Mount D1 and D2 in close proximity
- 1% linearity to 1 kHz

High Efficiency Crystal Oven Controller

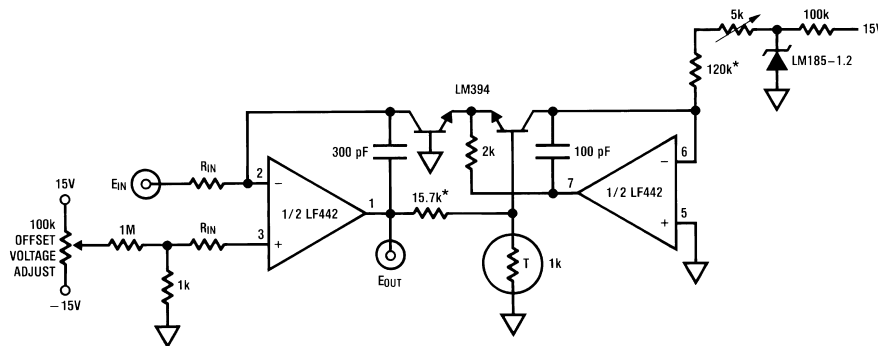


00915513

- $T_{control} = 75^{\circ}C$
- A1's output represents the amplified difference between the LM335 temperature sensor and the crystal oven's temperature
- A2, a free running duty cycle modulator, drives the LM395 to complete a servo loop
- Switched mode operation yields high efficiency
- 1% metal film resistor

Typical Applications (Continued)

Conventional Log Amplifier



00915514

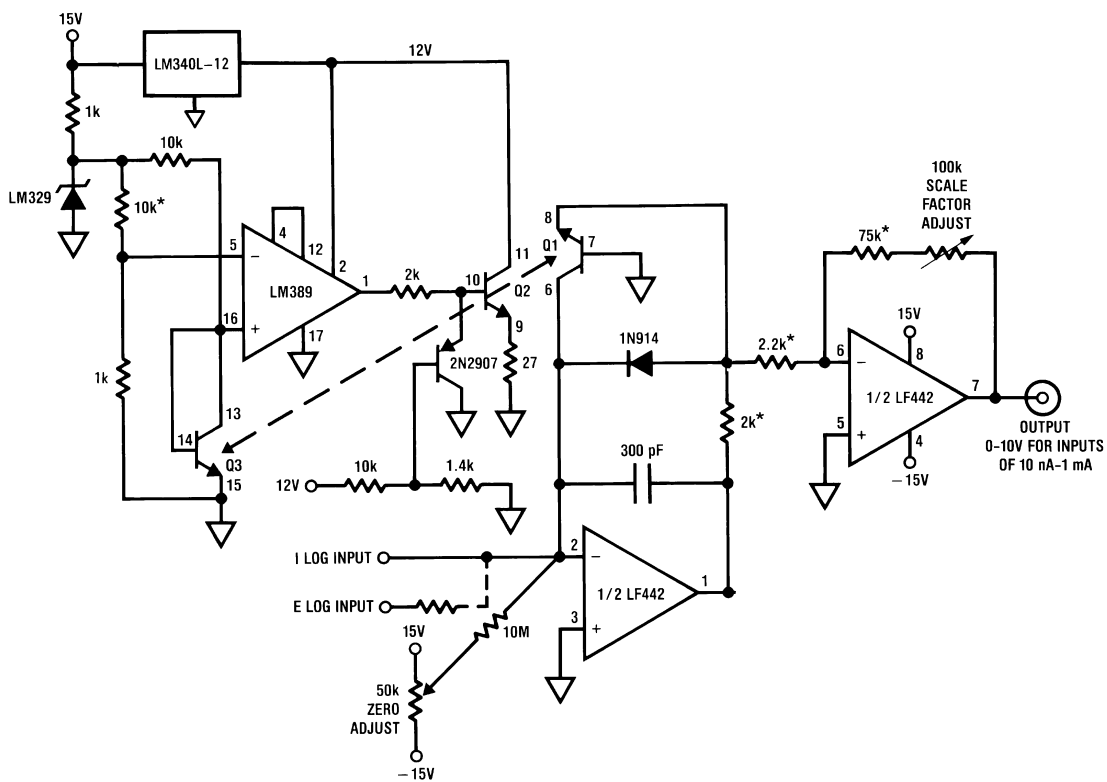
$$E_{OUT} = - \left[\log_{10} \left(\frac{E_{IN}}{R_{IN}} \right) + 5 \right]$$

R_T = Tel Labs type Q81

Trim 5k for 10 μA through the 5k-120k combination

*1% film resistor

Unconventional Log Amplifier

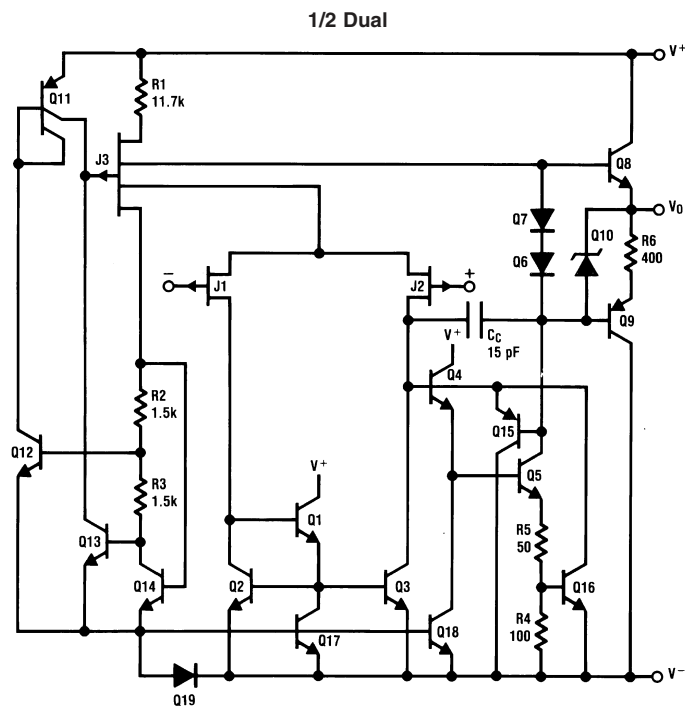


00915515

Q1, Q2, Q3 are included on LM389 amplifier chip which is temperature-stabilized by the LM389 and Q2-Q3, which act as a heater-sensor pair.

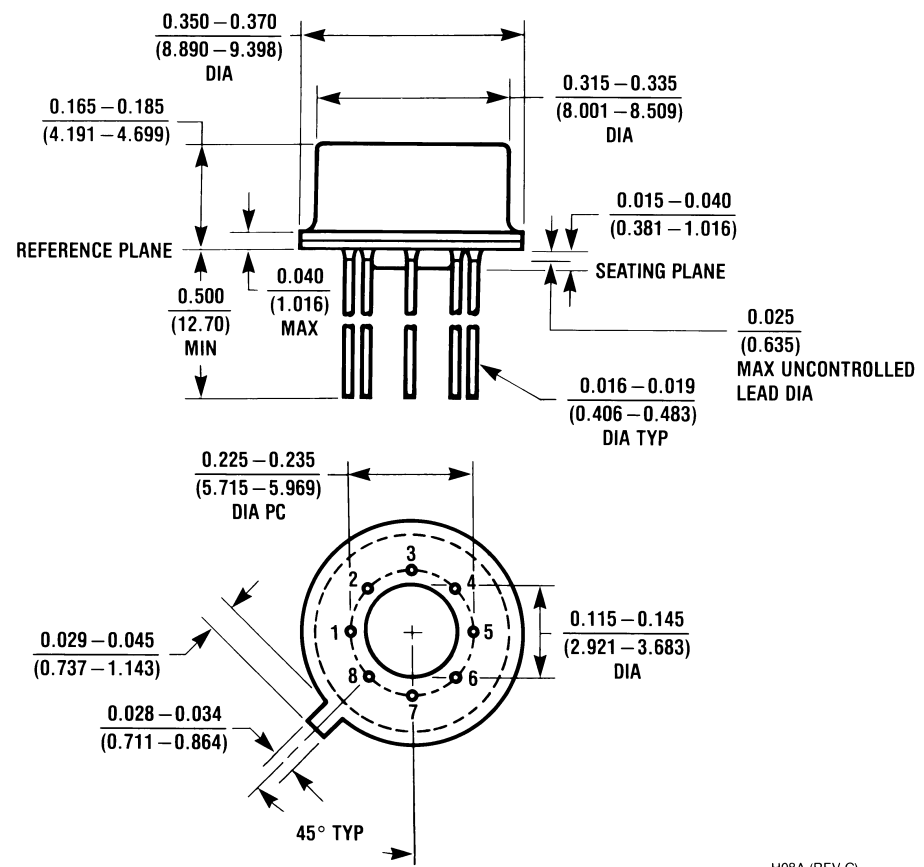
Q1, the logging transistor, is thus immune to ambient temperature variation and requires no temperature compensation at all.

Detailed Schematic



00915516

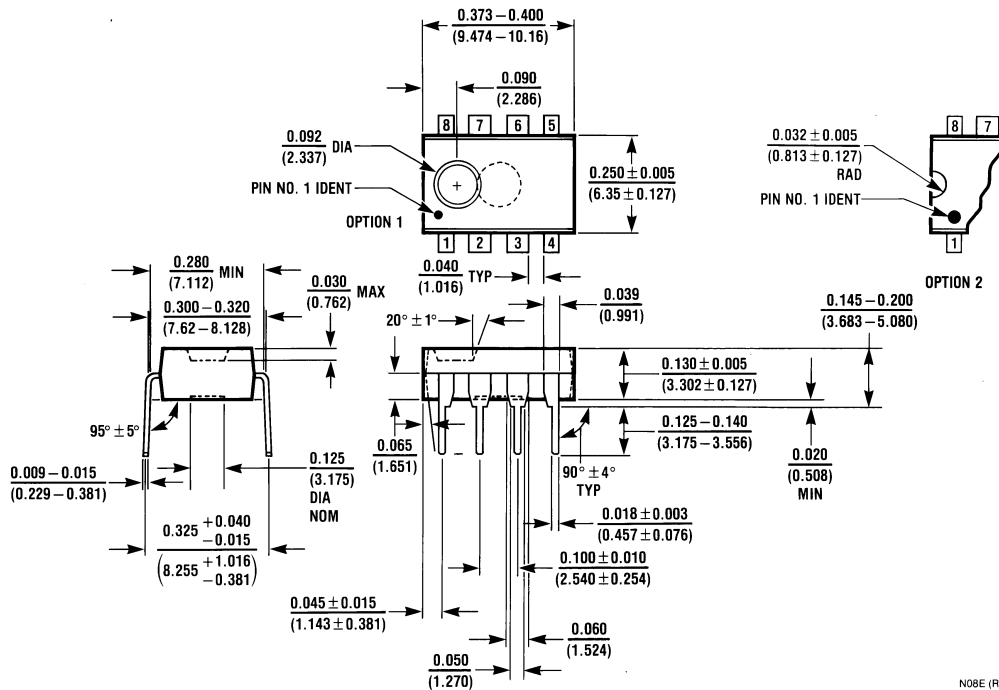
Physical Dimensions inches (millimeters)
 unless otherwise noted



TO-5 Metal Can Package (H)
 Order Number LF442AMH or LF442MH/883
 NS Package Number H08A

H08A (REV C)

Physical Dimensions inches (millimeters) unless otherwise noted (Continued)



Molded Dual-In-Line Package (N)
Order Number LF442ACN or LF442CN
NS Package Number N08E

N08E (REV F)


LIFE SUPPORT POLICY

NATIONAL'S PRODUCTS ARE NOT AUTHORIZED FOR USE AS CRITICAL COMPONENTS IN LIFE SUPPORT DEVICES OR SYSTEMS WITHOUT THE EXPRESS WRITTEN APPROVAL OF THE PRESIDENT AND GENERAL COUNSEL OF NATIONAL SEMICONDUCTOR CORPORATION. As used herein:

1. Life support devices or systems are devices or systems which, (a) are intended for surgical implant into the body, or (b) support or sustain life, and whose failure to perform when properly used in accordance with instructions for use provided in the labeling, can be reasonably expected to result in a significant injury to the user.
2. A critical component is any component of a life support device or system whose failure to perform can be reasonably expected to cause the failure of the life support device or system, or to affect its safety or effectiveness.

BANNED SUBSTANCE COMPLIANCE

National Semiconductor certifies that the products and packing materials meet the provisions of the Customer Products Stewardship Specification (CSP-9-111C2) and the Banned Substances and Materials of Interest Specification (CSP-9-111S2) and contain no "Banned Substances" as defined in CSP-9-111S2.

 **National Semiconductor**
Americas Customer Support Center
 Email: new.feedback@nsc.com
 Tel: 1-800-272-9959

National Semiconductor
Europe Customer Support Center
 Fax: +49 (0) 180-530 85 86
 Email: europe.support@nsc.com
 Deutsch Tel: +49 (0) 69 9508 6208
 English Tel: +44 (0) 870 24 0 2171
 Français Tel: +33 (0) 1 41 91 8790

National Semiconductor
Asia Pacific Customer Support Center
 Email: ap.support@nsc.com

National Semiconductor
Japan Customer Support Center
 Fax: 81-3-5639-7507
 Email: jpn.feedback@nsc.com
 Tel: 81-3-5639-7560

www.national.com